ACS NANO

www.acsnano.org

ARTICLE

Single-vesicle Tracking of α-Synuclein Oligomers Reveals Pore Formation by a Three-Stage Model

Bo Volf Brøchner, Xialin Zhang, Janni Nielsen, Jørgen Kjems, Daniel E. Otzen,* and Mette Galsgaard Malle*

Cite This: *ACS Nano* 2025, 19, 32108–32122

Read Online

ACCESS | Metrics & More | Article Recommendations | Supporting Information

ABSTRACT: **Neurodegenerative disorders, such as Parkinson's disease (PD) pose significant health challenges. A major hallmark of PD is the aggregation of α-synuclein into toxic oligomers (αSO) and fibrils. While many efforts focus on slowing disease progression, the molecular origins and mechanisms of αSO toxicity remain poorly understood, particularly regarding its proposed link to membrane disruption. To address this, we have developed a single-vesicle analysis platform for direct, and real-time measurements of αSO and membrane interaction. This platform allows us to demonstrate real-time translocation of dyes through αSO pores with single-particle resolution and use single-channel electrical recordings to analyze pore formation in planar lipid bilayers. Across methods, our data provide evidence for a three-stage model of αSO and membrane interactions, comprising initial membrane recruitment followed by partial pore insertion and subsequent full pore formation. Notably, while αSO recruitment was found to favor curved membranes, pore formation occurred more efficiently in less curved membranes, hence, recruitment is decoupled from a membrane charge-promoted reorientation and pore integration. Single αSO pore formations undergo multiple translocation steps making pore formation highly dynamic, cycling back and forth between partial insertion and full pore formation. The dynamic nature of pore formation can be modulated by lipid charge, lipid headgroup class, and ligand binding. Our findings suggest that increased dynamic pore formation could imply increased membrane toxicity. Evidence for the three-stage model is important for developing future targeting strategies to block αSO-mediated PD-related cellular dysfunction. We envision that the single-vesicle assay will enable screening of ligands modulating the pore formation.**

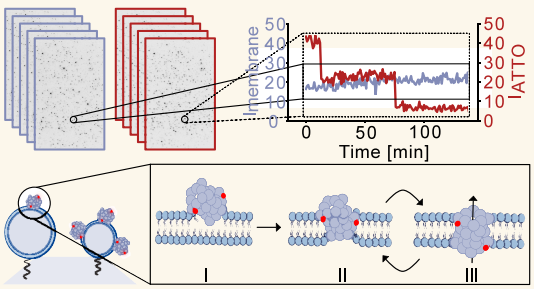

KEYWORDS: *Parkinson's disease, alpha synuclein oligomers, membrane interactions and pore translocation, three-stage pore formation, single-vesicle measurements*

INTRODUCTION

Membrane integrity is fundamental to cellular survival, serving as both a barrier and a dynamic platform for biological processes, such as signaling, trafficking, and energy transduction. Membrane disruption can severely compromise cellular function, particularly in neurodegenerative diseases, where membrane damage has been implicated in the loss of neuronal function and cell death.[1−3] Related to this, aggregation of the protein α-synuclein (α-Syn) is central to both disease pathology and progression in the common neurodegenerative disorder Parkinson's disease (PD) and other synucleinopathies. α-Syn is an intrinsically disordered protein hypothesized to be involved in synaptic vesicle regulation and trafficking.[4] However, misfolding and aggregation of α-Syn are associated with the formation of pathological protein inclusions called Lewy bodies[5] as well as soluble α-Syn oligomers (αSOs). These oligomers are considered a key factor in membrane disruption and subsequent neuronal dysfunction, being more cytotoxic per mass than the more well-characterized fibrillar species.[6] While αSOs have been shown to compromise lipid membrane integrity, the mechanism of this event remains poorly understood.[7−9]

The intrinsic heterogeneity of αSOs poses a significant challenge to elucidating the structure−function relationship. Unlike fibrils, which are highly uniform and give rise to

Received: March 6, 2025
Revised: July 23, 2025
Accepted: July 24, 2025
Published: August 12, 2025

https://doi.org/10.1021/acsnano.5c04005
ACS Nano 2025, 19, 32108−32122

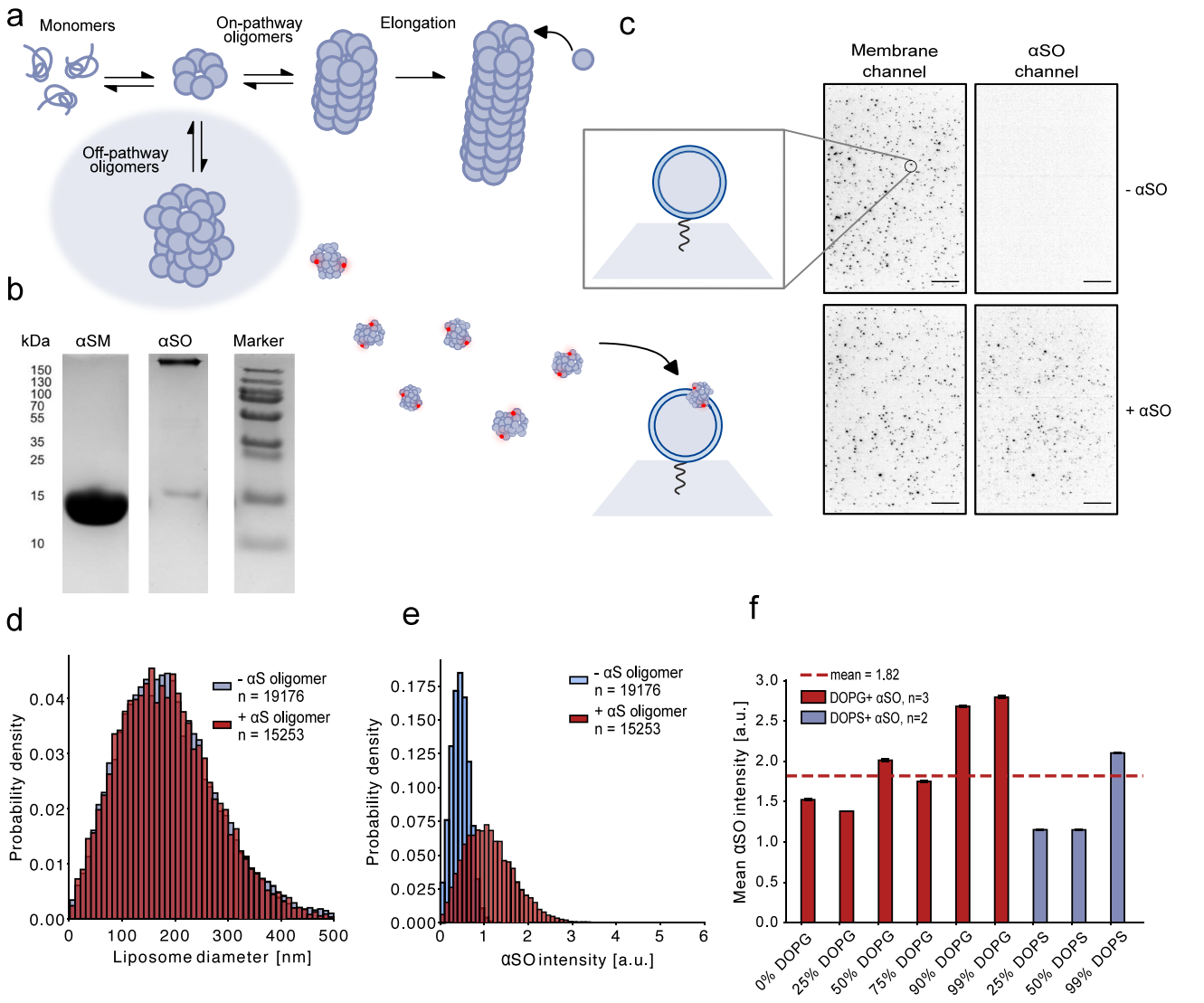

Figure 1. Single liposome detection shows charge-dependent recruitment of a cytotoxic off-pathway αSO. (a) Schematic representation of α-Syn aggregation. Derived from an initial aggregation model event, cytotoxic off-pathway αSO can be formed that do not continue their fibrillation to form fibrils. (b) SDS-PAGE of purified monomeric α-Syn and off-pathway toxic αSO. (c) Single-particle assay for αSO recruitment. Biotinylated liposomes are immobilized on a passivated glass surface where an incorporated lipidated-fluorescent dye in the liposome membrane allows detection of it in the membrane channel. In the bottom panels fluorescently labeled αSO is added and can be detected in the αSO channel. Colocalization of the two channels allows for quantification of the amount of αSO bound to each single liposome. (d) Histogram showing no change in liposome size distribution before and after the recruitment of αSO. (e) Histogram showing a clear intensity shift in αSO intensity before (blue background signal) and after the addition of αSO (red). (f) αSO associations to more than half a million single liposome membranes in response to increasing charge (increasing DOPG content) and different lipid composition (DOPS and DOPG lipids). Data is recorded in $n = 3$ biological replicates for DOPG vesicles and $n = 2$ for DOPS vesicles, error bars show the error propagated SEM. The distributions show distinct, though not statistically significant, levels of recruitment.

atomically resolved structures, αSOs exist as a diverse population with varying sizes, conformations, and toxic potential.[6,10,11] Generally, αSOs can be subdivided into two distinct types: "on-pathway oligomers", which act as intermediates in fibril formation, and "off-pathway oligomers" which arise through an alternative process that does not lead to fibril formation.[6,12−14] In vitro studies have produced αSOs in both subdivisions, with distinct structural and functional properties depending on the conditions under which they form. This variability, on top of the intrinsic heterogeneity, has hindered the development of a unifying model for how αSO-membrane interactions drive toxicity. This study focuses on the toxic off-pathway oligomer, which forms spontaneously during fibrillation and accumulates as a stable and toxic species that does not lead to fibrils. Hence, they are believed to be physiologically relevant and likely present in the brains of patients with PD.[7,15,16] Given the cytotoxicity of αSO, identifying high-affinity ligands for therapeutic and diagnostic applications is of great interest. One example of small ligands is nanobodies (NBs). NBs are modified variable domains derived from the heavy chain-only antibodies, a distinct type of antibodies found in camelids.[17,18] These have been suggested to have great therapeutic potential due to their stability, high specificity, and hypothesized ability to cross the blood-brain barrier.[19,20] We have recently produced two different NBs with high affinity and specificity for the αSO species.[21]

Previous studies have demonstrated that αSOs preferentially target negatively charged lipid membranes, such as those

https://doi.org/10.1021/acsnano.5c04005
ACS Nano 2025, 19, 32108−32122

containing phosphatidylglycerol (PG) or phosphatidylserine (PS), over neutral lipid membranes like phosphatidylcholine (PC).[7−9,22−26] Negatively charged lipids are abundant in neuronal membranes, particularly in synaptic vesicles, which are rich in PS, and mitochondrial membranes, which predominantly contain PG. This makes these systems particularly relevant to PD pathology. Interestingly, while PS-containing membranes bind α-Syn efficiently, they exhibit less membrane leakage than PG-containing membranes.[9,23,24] This paradox underscores the complexity of lipid-specific interactions and suggests that membrane disruption is influenced not only by charge but also by curvature and headgroup structure.

αSO-driven membrane disruption is speculated to involve partial insertion into lipid bilayers, leading to their destabilization and allowing leakage of ions or other molecules.[7,9,22−24,27] However, the details of this process, including how lipid composition and curvature modulate this disruption, remain unclear. Most studies rely on bulk techniques, such as the release of fluorescent dyes or ions from large unilamellar vesicles (LUVs) or small unilamellar vesicles (SUVs).[7−9,22−25] While these methods provide valuable insights, they average out the unavoidable heterogeneity from both the membrane vesicles and the inherently diverse αSO species, failing to capture the real-time dynamics and individual steps of membrane disruption.[26,28] Single-vesicle techniques are essential for addressing these limitations. Total internal reflection fluorescence (TIRF) microscopy technique allows real-time observation of protein−membrane interactions at the single-vesicle level.[28,29] This bypasses ensemble averaging, revealing transient events and unraveling heterogeneous behavior otherwise invisible in bulk measurements.

Here, we report a single-liposome assay for direct and real-time measurement of αSO and membrane interaction. We have screened over 500,000 individual liposome-αSO interactions, providing the basis to build a biophysical understanding of the interactions in unprecedented detail. We propose a three-step model for αSO and membrane interactions consisting of initial membrane recruitment, partial insertion, and subsequent full pore formation. Recruitment preferentially occurs on membranes with high curvature, while pore formation is favored on membranes with lower curvature and less tension. Pore formation is observed to be highly dynamic, cycling back and forth between partial insertion and full pore formation, which is modulated by charge, lipids, and αSO-binding nanobodies. Our findings set the stage for future mechanistic investigations of αSO-membrane interactions and provide a platform for screening oligomer-membrane and ligand interactions, overcoming inherent heterogeneity. Understanding the modulable and dynamic nature of pore formation might pave the way to mitigate αSO-induced membrane dysfunction.

RESULTS AND DISCUSSION

Direct Observation of Charge-Promoted Recruitment of Individual αSOs to Single-Liposome Vesicles. To address how individual αSOs interact with lipid membranes, we established a single-vesicle assay and exposed it to the cytotoxic off-pathway αSO species (Figure 1a) which forms spontaneously during aggregation-inducing conditions and is known to form a pore-like structure.[7,13,30,31] Previous studies of this αSO species have characterized it using Fourier Transform Infrared Spectroscopy (FTIR), Small-Angle X-ray Scattering (SAXS), and Circular Dichroism (CD), revealing a compact, antiparallel β-sheet-rich core and a disordered outer region comprising the N-terminus of the protein. These αSOs are unable to elongate fibrils and are thus believed to be off-pathway.[15,32] To confirm the correct αSO species, αSOs were isolated from monomeric species and other αSO variants using size exclusion chromatography.[33] They appeared as a large species (∼450 kDa) presenting as a distinct band on an SDS-PAGE gel, and were further verified by a dot blot analysis (Figure 1b and Supplementary Figures 1−2).

Next, we produced SUVs (liposomes) containing 0.5% DSPE-PEG(2000)-Biotin, allowing us to tether them onto a PLL-*g*-PEG-biotin-covered glass surface via a neutravidin linker. The liposomes also contained 0.5% ATTO−DOPE, allowing imaging with a high signal-to-noise ratio using total internal reflection microscopy (TIRF). Forty-eight micrographs were taken before and after the addition of ATTO655-labeled αSO (Figure 1c). A total of 578,863 liposomes were analyzed across three biological replicates. Figure 1c shows a representative field of view of both the liposome channel and the αSO channel before and after the addition of the αSOs, clearly demonstrating the membrane association of the αSOs. All liposomes were analyzed by signal integration to extract both nanometer-precise localization and membrane intensity using custom Python software. The single-vesicle membrane intensity units were converted to liposome diameters from the mean integrated intensity normalized to the mean vesicle size from nanoparticle tracking analysis (NTA) of the suspended liposome for each liposome preparation (Supplementary Figure 3).[28,34] Measurements of the size distribution of liposomes showed no change upon addition of αSO (Figure 1d and Supplementary Figures 4−5). The vesicle localization software allowed us to colocalize all membrane-associated αSO signals, enabling quantification of αSO binding to each liposome.

Here, we integrated the αSO signal and compared the intensity distributions before (blue) and after (red) the addition of labeled αSO. Using a Kolmogorov−Smirnov test (KS-test), we found a significant shift in the signal distributions after αSO recruitment (Figure 1e and Supplementary Figures 6−7). When no liposomes were tethered to the glass slide, we saw no αSO bound to the surface, demonstrating that binding is membrane-dependent, and our assay has minimal false positive associations or membrane signal integration (Supplementary Figure 8).

To test the charge-dependent membrane recruitment of αSO, we prepared a series of increasingly anionic liposomes, containing 0−99% DOPG and 0−99% DOPS. A clear trend of increased recruitment with negative charge was observed (Figure 1f). However, neutrally charged membranes (0% DOPG) still distinctly recruit αSO. DOPS liposomes showed lower recruitment compared to DOPG liposomes, indicating the importance of the lipid headgroup. Additionally, DOPS membranes exhibited more cooperative (all-or-nothing) behavior, with highly significant elevated recruitment at 99% DOPS. This is consistent with calcein-release assays, where membranes with greater negative charge display higher dye release, and vesicles containing DOPG/POPG are more destabilized by αSO than those containing DOPS/POPS.[7−9,22−25]

Membrane Charge- and Curvature-Promoted Recruitment of αSO. A mechanistic understanding of αSO recruitment requires deconvolution of lipid composition,

https://doi.org/10.1021/acsnano.5c04005
ACS Nano 2025, 19, 32108−32122

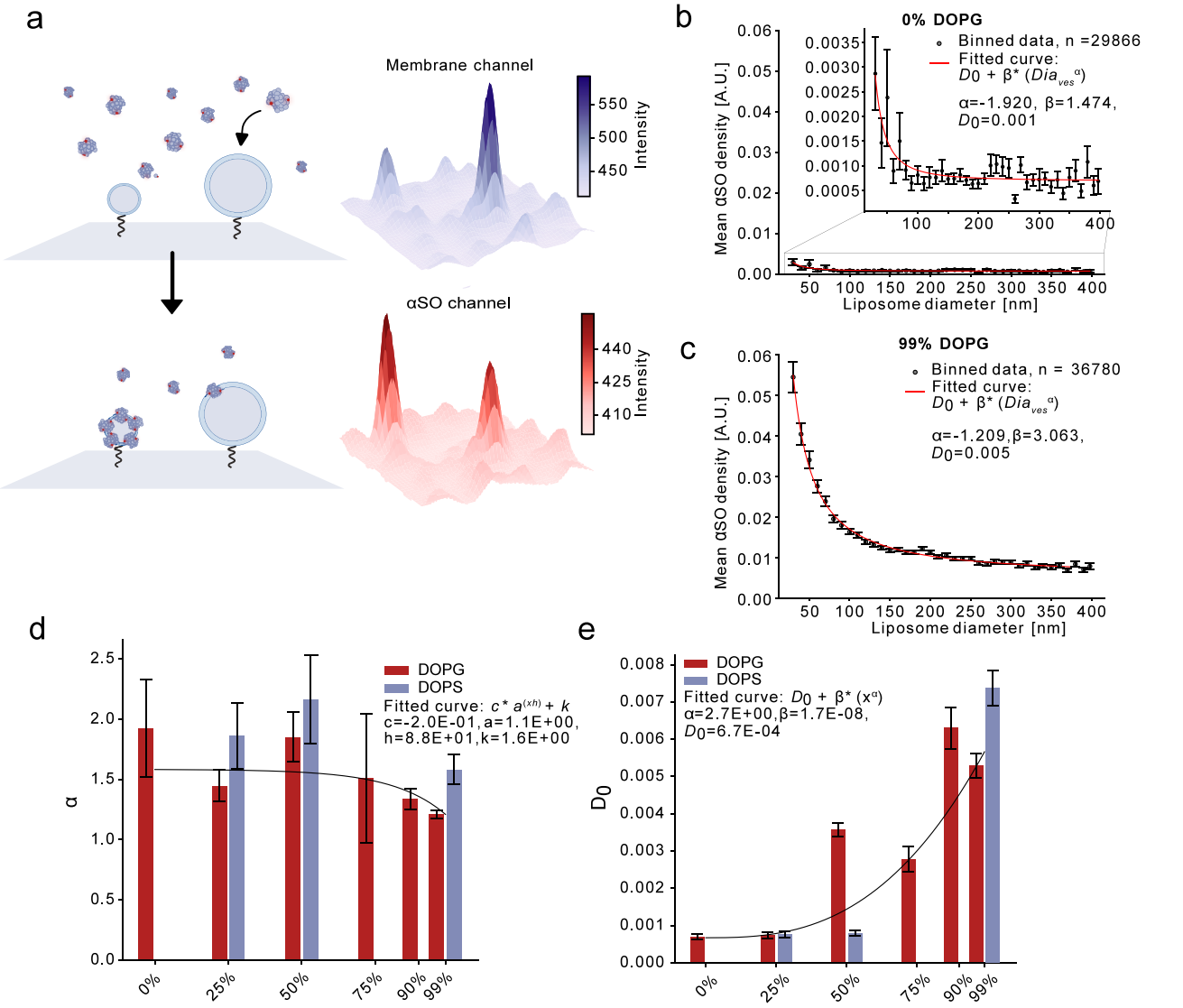

Figure 2. Single vesicle detection shows higher αSO density with increasing curvature. (a) Colocalization of immobilized liposomes and associated αSO enable direct measurement of the amount or density of αSO per liposome. The inevitable heterogeneous liposome size distribution allows for screening of membrane-dependent behavior such as curvature. Representative images in c and d show larger liposomes, hence less curved, display lower αSO density. (b) Liposome diameter as a function of membrane density of αSO for liposomes with 0% DOPG. The relation is fitted to a recruitment power function ($D = D_0 \cdot \beta \cdot (Dia_{vesicle})^{\alpha}$) showing a decrease in recruited density for increasing liposome size. The inset shows the steep growth rate recruitment for small liposomes. (c) Liposome diameter plotted against membrane density of αSO for liposomes with 99% DOPG. The relation is fitted to a power function which shows a decrease in recruited density for increasing liposome size. However, this shows a less strong power function dependency than for the 0% DOPG liposomes. The data in (b, c) is binned per liposome size for each 10 nm with error bars showing the SEM. (d) Liposomes with increasing charges for both DOPG and DOPS vesicles are all measured at a single-vesicle level and fitted to the recruitment's power function. The exponent of the fit α, which refers to the strength of the recruited density for curvatures, depicts a negative correlation for increasing anionic membrane charge. Hence, lower-charged vesicles are more curvature-dependent in the recruitment of αSO. (e) Density offset from the recruitment's power function for increasing charges for both DOPG and DOPS vesicles shows an increasing offset upon increasing membrane charge. The data suggest that the higher charged liposomes overall recruit more αSO, but the recruitment is less dependent on curvature. Error bars in (d, e) show std.

charge, and curvature, which are averaged out due to heterogeneity in bulk studies. Our single-vesicle analysis addresses this limitation by resolving the relationship between individual liposome sizes (Figure 2a) and αSO recruitment, enabling us to screen membrane properties and transform molecular stochasticity into an experimental advantage. Here, surface-tethered liposomes were integrated in the membrane intensity channel and colocalized with the membrane-bound αSO signal, enabling the calculation of αSO density for each liposome and its curvature (Figure 2a), given the inverse relationship between curvature and vesicle diameter.[35,36] This allowed us to screen single curvature dependent recruitment quantified across three biological replicates, yielding a total of 362,787 liposomes (Figure 2b,c and Supplementary Figures 9–10). Here, the αSO density ($D_{\alpha SO}$) was plotted against liposome size ($Dia_{vesicle}$), binned at 10 nm intervals ranging from 25 to 400 nm in diameter, and fitted using an offset power function: $D_{\alpha SO} = D_0 + \beta \cdot (Dia_{vesicle})^{\alpha}$, for each membrane

https://doi.org/10.1021/acsnano.5c04005
ACS Nano 2025, 19, 32108–32122

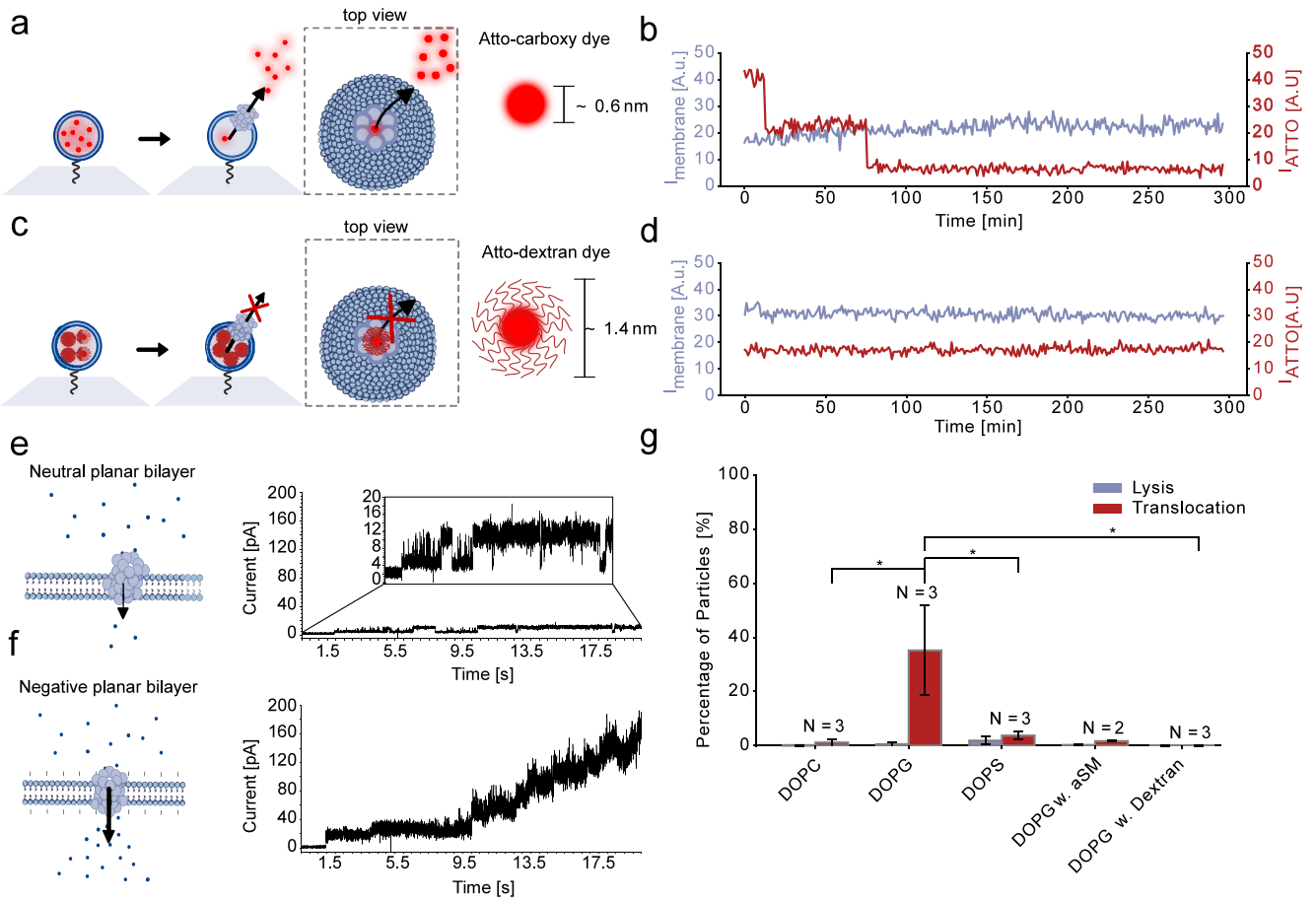

Figure 3. Real-time single-vesicle fluorescent and single-channel electrical recordings demonstrating αSO pore formation and small-molecule translocation. (a) Liposomes are membranes labeled with ATTO488-DOPE and ATTO655 carboxy are encapsulated, allowing simulations and real-time recording of both the membrane and the lumen dyes using a TIRF microscope. αSOs were injected into the microscope chamber after 10 frames of recording. (b) Representative time trajectories were obtained from real-time tracking and integration of both the membrane (blue) and lumen dye (red) intensities. Here, the trajectory shows a stable liposome membrane and a dynamic pore formation with two distinct open pore formations, which allows for the translocation of dyes. (c) Liposomes are membrane labeled with ATTO655-DOPE and the larger ATTO 488-dextran 4 kDa dye was encapsulated. (d) Representative time trajectories displaying a stable membrane and no translocation of ATTO 488-dextran. (e) Representative current trace showing the partial insertion of αSO into neutral planar lipid bilayers. Prior to recording, 96.8 nM of αSO was added to each side of the chamber. The neutral-charged planar lipid bilayer was formed using DphPC. (f) Representative current trace showing the full insertion of αSO into negative-charged planar lipid bilayers. Prior to recording, 96.8 nM of αSO was added to each side of the chamber. The negative-charged planar lipid bilayer was formed using DphPG. (g) Statistics from thousands of single liposome tracking, as explained in (b, d). Interestingly the activity of αSO in charged 99% DOPG vesicles shows a significant elevated pore formation. The monomer shows no pore activity, which is confirmed by electrical recordings. Finally, the translocation of dextran is not present, suggesting the translocation is through the small pore-like structure of the αSO. Asterisks (*) in (g) indicate a *p*-value <0.05 and reflect a significant difference based on a Mann−Whitney *U* test.

condition. The exponent α is the rate of curvature dependency, D_0 is the density offset while the scaling factor β quantifies the αSO's sensitivity to curvature dependency.[34]

Neutrally charged liposomes showed a strong curvature promoted recruitment with a rate of curvature dependency factor $\alpha = -1.920 \pm 0.40$ (Figure 2b). The density offset value, $D_0 = 0.001 \pm 6.69 \times 10^{-5}$, reflects reduced binding to flatter membranes and an overall low αSO density. The high α and low D_0 values reflect low αSO recruitment on less curved, neutral membranes, consistent with the reported lack of binding to GUVs.[24] Negatively charged membranes (99% DOPG) showed a significantly higher density offset value, $D_0 = 0.005 \pm 0.0003$ (Figure 2c) reflecting a significantly stronger αSO recruitment. Surprisingly, the curvature dependency (α) is significantly lower for negatively charged membranes, with $\alpha = -1.209 \pm 0.033$. Overall αSO recruitment depends on D_0, α, and β, quantified by integrating the αSO density across all liposomes. For 99% DOPG liposomes, the integral is 5.296, whereas neutrally charged liposomes exhibit a substantially lower value of 0.451. To fully investigate the charge-dependent single-vesicle recruitment of αSO, we prepared a series of increasingly anionic liposomes, containing 0−99% DOPG and 0−99% DOPS (Supplementary Figures 9−10) and extracted α and D_0 values to compare the curvature-promoted recruitment across the membrane compositions (Figure 2d,e). Here, the curvature dependency (α) for DOPG-containing liposomes follows an exponential decrease with increasing anionic charge, demonstrating that neutrally charged membranes are more curvature-dependent, with this dependency decreasing exponentially as negative charge increases. DOPS liposomes showed stronger curvature-promoted recruitment, which is particularly evident at a high negative charge, with 99% DOPG

https://doi.org/10.1021/acsnano.5c04005
ACS Nano 2025, 19, 32108−32122

exhibiting an α-value of -1.209 ± 0.033, compared to the significantly higher α-value of 1.580 ± 0.123 for 99% DOPS. Despite this disparity, DOPS vesicles show a similar overall trend, with curvature dependency decreasing as membrane charge increases. The offset density (Figure 2e) increases with membrane charge for both lipid compositions, following a power-law correlation and demonstrating steep charge-dependent recruitment. DOPS liposomes exhibit a steeper increase in offset, indicating a stronger and more cooperative charge dependency compared to DOPG liposomes.

The recruitment of αSO resembles the recruitment and binding behavior of α-Syn monomers, which are known to be sensitive to both membrane curvature and lipid headgroup composition.[32,37−41] Upon interacting with membranes, the N-terminus of the monomer adopts an α-helical structure that is crucial for membrane binding. Notably, the N-terminus is part of the disordered outer region of the oligomer, suggesting that the interaction may be driven by a similar mechanism as in the monomer. This is supported by previous studies showing that deletion of the N-terminal region leads to reduced αSO recruitment.[32]

To our knowledge, this is the first quantitative description of αSO recruitment using single-vesicle measurements, avoiding ensemble averaging and enabling direct comparison of lipid headgroup, charge, and curvature effects. Our data demonstrate that neutral membranes can recruit αSO, but recruitment is highly curvature-promoted, likely due to lipid packing defects exposing hydrophobic tails. Recruitment significantly increases with higher anionic membrane content. However, our findings indicate that lipid headgroup also plays an important role, as αSO recruitment to DOPS membranes is more sensitive to charge and curvature compared to DOPG membranes.

Single-Vesicle Fluorescent and Single-Channel Electrical Recordings Show αSO Pore Formation and Small-Molecule Translocation. To gain deeper insight into the interaction between αSOs and lipid membranes, we employed a single-vesicle setup to directly measure how αSOs permeabilize or perforate membranes. While previous studies have demonstrated that αSOs induce leakage or disruption, particularly in anionic vesicles, these findings are based on bulk measurements that cannot disentangle specific interaction mechanisms, such as lysis or pore formation, or elucidate the precise nature or kinetics of the insertions.[7,24] To address this limitation, we encapsulated ATTO-655 carboxy in 0.5% ATTO-488-DOPE membrane-labeled liposomes, enabling synchronous recording of both vesicle membrane and lumen dye (Figure 3a). Liposomes were immobilized and recorded for 5 h with a temporal resolution of 1 frame per minute. After 7 min, (0.31 μM αSO corresponding to 0.01 μM αSO concentration) was added using an automated peristaltic pump setup. In-house automated software was used to track and extract spatiotemporal information for individual liposome monitoring, each membrane and its lumen molecules. Notably, as seen in intensity-time trajectories (Figure 3b) the membrane signal (blue) remained stable throughout the 5-h observation period, while the lumen dyes showed two distinct step-like events, occurring at 15 and 75 min for this particular particle, indicating initial full pore insertion followed by a partial insertion, then reverting to full insertion, resulting in two subsequent dye translocation steps. This indicates that lumen dye release is mediated by αSO insertion and pore formation in the membrane, while liposome membranes retain structural integrity [Supplementary Figure 11 for additional trajectories].

To confirm that only small molecules can translocate through αSO pores, we loaded liposomes with ATTO 488-dextran, a dye with a hydrodynamic diameter of approximately 1.4 nm (Figure 3c). A representative trajectory in Figure 3d shows stable intensity in both liposome membrane (blue) and encapsulated cargos (red) over a 5-h observation period, indicating no translocation of the larger molecule [Supplementary Figure 12 for additional trajectories]. This suggests that larger molecules exceed the dimension of αSO pores, consistent with pore formation of a defined size rather than random permeabilization. Additionally, we measured the translocation of ATTO655 carboxy in the presence of αS monomers. Here, liposomes remained stable, and no dye translocation was observed (Supplementary Figure 13), similar to the buffer-only control (Supplementary Figure 14). A higher temporal resolution was applied as a control to provide additional evidence for pore formation. This allowed us to resolve the translocation dynamics of the encapsulated dye, which followed an exponential decay characteristic of pore-mediated release (Supplementary Figure 15). To further support the presence of both fully and partially inserted pores, we performed an additional control experiment. We imaged encapsulated dye together with 1 nM labeled αSO (10-fold diluted) to confirm that the observed stepwise dye translocation was not due to αSO binding and unbinding from the liposomes. The data showed a steady αSO signal between translocation events, confirming that the stepwise release reflected distinct pore insertion states rather than fluctuations in αSO binding (Supplementary Figure 16). Collectively, these results demonstrate that molecular translocation indeed occurs through the αSO pore.

To further confirm αSO pore formation, we employed a technique using single-channel electrical recording setup on planar lipid bilayers.[42,43] On a neutral planar lipid bilayer (using DphPC). Here, αSO perforation led to ionic flux with an open pore current of 7.67 ± 2.08 pA at an applied voltage of 20 mV, which indicated the formation of small pores. A characteristic current−time trajectory representing αSO insertion into a neutral lipid bilayer is shown in Figure 3e (Supplementary Figures 17−19). The amplified current trace showed a single-step current increase, indicating limited pore insertion activity of αSO in a neutral lipid membrane. In contrast, the same amount of αSO (96.8 nM) induced a stepwise current increase, causing higher ionic conductivity in negatively charged bilayers (DphPG) (Figure 3f and Supplementary Figures 20−22). The pore formation is further supported by a reproducible conductance of ∼300 pS across multiple recordings, as well as a linear I−V curve following insertion, consistent with Ohmic behavior (Supplementary Figure 23). This observation suggests that αSO more efficiently inserts itself into negatively charged lipid membranes. Interestingly, the presence of $CaCl_2$ did not significantly influence αSO pore insertion activity in either neutral or negatively charged planar lipid bilayer (Supplementary Figures 18 and 21). Furthermore, control experiments using the same amount of αS monomers (96.8 nM) on the negatively charged bilayer showed no insertion activity, confirming that the observed increase in ionic conductivity was specifically due to αSO pore formation (Supplementary Figure 24).

https://doi.org/10.1021/acsnano.5c04005
ACS Nano 2025, 19, 32108−32122

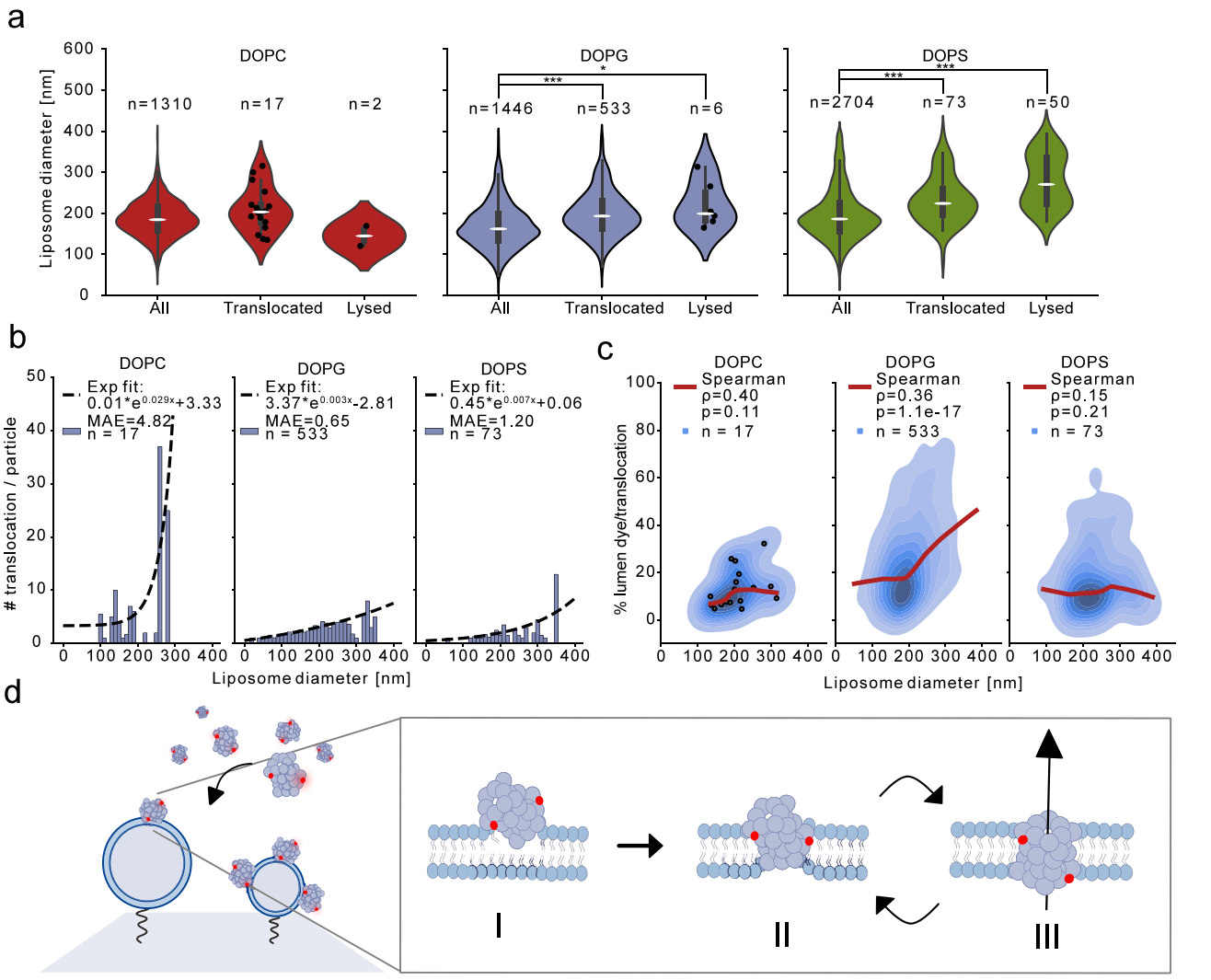

Figure 4. Single-vesicle recording shows αSO pore activity is regulated by the membrane lipids. (a) Distributions of αSO pore activity for neutral DOPC and charged DOPG and DOPS liposomes plotted against the liposome diameter. For the neutral DOPC liposomes (red), no curvature or size preference was found and only 0.65 and 0.08% of the liposomes were observed to have αSO pore translocations of dyes or lysed in the presence of αSO, respectively. For negatively charged DOPG liposomes (blue), pore-forming events were highly significantly shifted toward larger liposomes with lower curvature. A subset of the liposome population underwent lysis, also predominantly among larger liposomes. In contrast, DOPS (green) liposomes exhibited a smaller fraction of pore-forming events, though this fraction is likewise significantly enriched in larger liposomes. Lysis was more prevalent in DOPS liposomes and is similarly associated with larger liposomes. Asterisks indicate the following *p*-values with significance * = 0.05, ** = 0.01, * = 0.005 based on a one-sided Mann−Whitney *U* test. (b) Quantification of the number of step-like translocations of dyes through the αSO pores. Here DOPG vesicles showed a linear distribution of the number of leaks per liposome. In contrast, DOPS and DOPC vesicles showed an exponentially increasing number regarding vesicle diameter. (c) The quantity of lumen dyes translocated in a single translocation event. DOPG vesicles show a positive correlation of % translocated with liposome diameter. For DOPS and DOPC liposomes we find no correlation. (d) Our results suggest a new three-stage model for αSO and membrane interactions with initial membrane recruitment preferably in smaller more curved vesicles followed by a reversible pore formation preferably in larger less curved membranes which strictly depends on membrane charge. Hence αSO recruitment to the membrane is decoupled from charge-dependent pore formation.**

To resolve the role of differently charged lipids in αSO pore insertion, we prepared 3 different types of liposomes using one neutrally charged (DOPC) and two anionic (DOPG and DOPS) lipids, encapsulated ATTO655-carboxy, and recorded in real time, yielding thousands of single-vesicle measurements (Supplementary Figure 25). In neutrally charged membranes, only a small fraction of vesicles exhibited translocation (1.14 ± 1.34%), and 0.18 ± 0.14% underwent lysis (Figure 3g). In contrast, vesicles with anionic DOPG membranes showed a dramatic increase in pore formation, with 35.16 ± 16.55% of vesicles exhibiting translocation, while only 0.52 ± 0.73% underwent lysis. Interestingly, anionic DOPS vesicles exhibited significantly lower pore insertion (3.71 ± 1.43% translocation), while a substantial fraction (1.83 ± 1.46%) underwent lysis, indicating a higher propensity for membrane disruption compared to DOPG vesicles. Real-time recordings with αSM revealed minimal activity, with 1.67 ± 0.04% of vesicles showing translocation and 0.24 ± 0.03% undergoing lysis. As a control, vesicles containing large dextran-coupled dye encapsulated in negatively charged DOPG membranes exhibited no detectable translocation (0.0 ± 0.0%), confirming that dye release occurs through αSO pores. Collectively, our

https://doi.org/10.1021/acsnano.5c04005
ACS Nano 2025, 19, 32108−32122

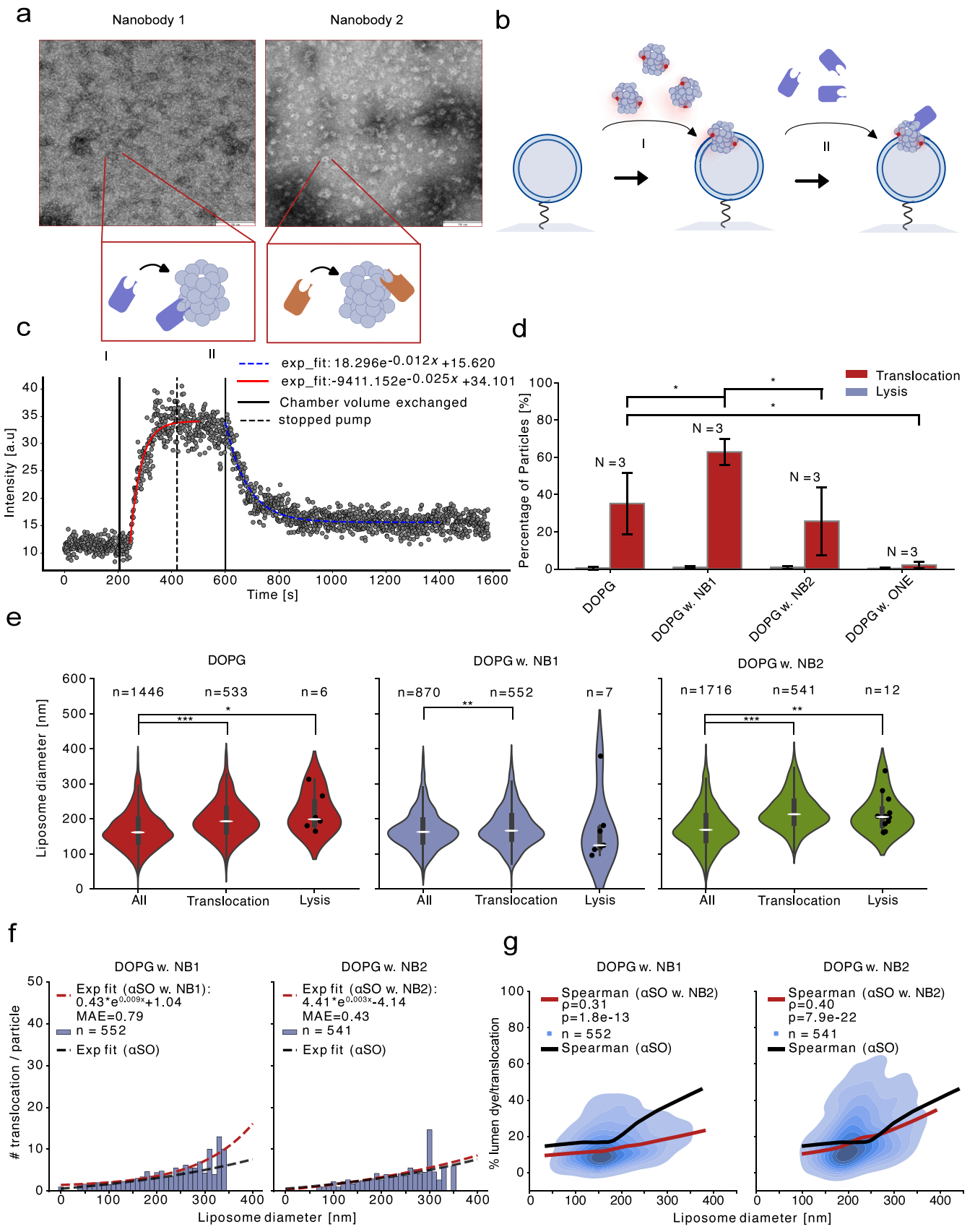

Figure 5. Nanobodies modulate the translocation of small molecules from the lumen. (a) nsTEM images confirming binding of NB1 and NB2 to αSO. (b) Schematic illustration of real-time imaging of nanobody binding to membrane-associated αSO. Fluorescently labeled αSOs are first injected into the microscope channel, followed by the injection of nanobodies. (c) Representative time trajectory of real-time recording of αSO recruitment followed by NB1 binding. (d) Statistics of αSO pore activity for DOPG vesicles with subsequent addition of either no nanobodies, NB1, or NB2, respectively. Additionally, we measured αSO pore activity for a chemically linked and stabilized αSO

https://doi.org/10.1021/acsnano.5c04005
ACS Nano 2025, 19, 32108−32122

Figure 5. continued

using ONE. Here the presence of NB1 results in a significant increase in activity and the stabilized ONE:αSO shows significantly less activity. (e) Distributions of αSO pore activity for DOPG liposomes with no nanobodies (red), NB1 (blue) or NB2 (green) present, plotted against the liposome diameter. The distribution of pore-forming events in absence of nanobodies (red) is highly significantly shifted toward larger liposomes. The addition of both NB1 and NB2 additionally shows that pore-forming events remain highly significantly shifted toward larger liposomes. Asterisks indicate the following p-values with significance * = 0.05, ** = 0.01, * = 0.005 based on a one-sided Mann−Whitney *U* test. (f) Quantification of the number of step-like translocations of dyes through the αSO pores. The presence of NB1 results in a more exponentially increasing distribution with liposome diameter than in the presence of NB2. (g) The quantity of lumen dyes translocated in a single translocation event. The presence of both NB1 and NB2 results in a positive correlation of % translocated with the liposome diameter.**

findings reveal that αSO can bind to both neutrally and negatively charged membranes, however, only the negative membrane charges activate pore formation. Additionally, we find subsequent step-like translocation of lumen dyes for single-vesicles. This suggests a novel three-stage interaction model involving initial αSO recruitment to the membrane surface, followed by cycling between partial insertion and full pore formation. While the mechanism of membrane permeabilization by αSOs remains debated,[8,44] our results, in agreement with previous studies, demonstrate that binding alone does not necessarily lead to membrane rupture.[24] Our data suggests that pore formation in SUVs the predominant mechanism over membrane lysis.

Dynamics of αSO Pore Formation Are Sensitive to Lipid Charge and the Headgroup Type. The time-resolved recording of dye translocation at the single-vesicle level allowed us to investigate the effect of lipid composition and curvature for αSO pore formation. Here we find that pore formation is highly dynamic at the individual oligomer level, cycling reversibly between partial insertion and full pore forming stages. We found that the dynamic or frequency of pore formation is sensitive to both lipid charge and headgroup type.

Again, we investigated neutral membranes (DOPC) and two types of anionic membranes (DOPG and DOPS), yielding thousands of vesicles. Each vesicle was classified as either (i) nonreacting, (ii) translocating (pore formation), or (iii) lysed (simultaneous lumen and membrane disruption). The classified events were plotted as a function of the liposome diameter (Figure 4a). Neutrally charged liposomes (red) showed no curvature preference for pore formation, however, it should be noted that the number of translocations was low, as negative charges are found crucial for active pore formation. Notably, for negatively charged DOPG liposomes (blue), pore-forming events are highly significantly shifted toward larger, lower-curvature liposomes (P-value = 5.6×10^{-30} based on a one-sided Mann−Whitney U (MWU) test and P-value = 4.4×10^{-16} based on a Kolmogorov−Smirnov (KS) test). A subset of the liposome population also underwent lysis, predominantly among larger liposomes (P-value = 0.01 MWU-test and P-value = 0.048 KS-test). In contrast, DOPS liposomes (green) show a smaller fraction of pore-forming events, however still predominantly in significantly larger liposomes with lower curvature (P-value = 1.2×10^{-08} MWU-test and P-value = 2.4×10^{-08} KS-test). Also, lysis is significantly associated with larger liposomes (P-value = 4.0×10^{-16} MWU-test and P-value = 2.4×10^{-08} KS-test).

Next, the time-resolved single-vesicle analysis provided insight into an important aspect of αSO-membrane interactions, namely the dynamics of pore formation, measured as the frequency of translocation events as a function of liposome size (Figure 4b). The observed time-resolved on/off pore formation suggests that the oligomer is first recruited to the membrane, followed by cycling back and forth between partial and full pore formation stages, which we can observe as on/off translocations through the pore. We observed that individual liposomes can undergo up to 37 cycling events between being partially and fully inserted, where larger liposomes show a higher number of translocations. DOPG vesicles showed a linear increase in the number of translocations with increasing liposome size, whereas DOPS and DOPC vesicles exhibited slightly exponential and more clearly exponential relationships, respectively. Furthermore, for each translocation event, we quantified the quantity of the lumen (Figure 4c). Here, DOPG vesicles showed a positive correlation between percent dye translocated and liposome diameter, indicating that larger liposomes release a greater proportion of dyes per translocation event (p-value = 1.1×10^{-17} based on Spearman correlation). This suggests the presence of larger or more stable pores in flat membranes. Conversely, DOPC and DOPS vesicles show no correlation in translocation as a function of liposome sizes. This might be due to reduced rotational or penetration freedom for the αSO due to less preferred membranes and charge. These findings suggest that pore formation is highly dynamic, with larger, less-curved liposomes exhibiting increased dynamic favorability. Moreover, pore formation is strongly lipid-dependent, being more pronounced in DOPG vesicles, where pores also appear to be more stable compared to those in DOPS vesicles. These findings might be of great biological relevance, as PG lipids are found in mitochondrial membranes, and PS lipids are found in synaptic vesicle membranes.[45] Our findings demonstrate that αSO recruitment is enhanced by high membrane curvature, likely due to increased lipid packing defects and the exposure of acyl chains facilitating initial membrane association. In contrast, pore formation is more efficient on flatter membranes, where reduced curvature and membrane tension suggest a mechano-sensitive process. Reduced curvature may provide a more symmetric environment and decreased leaflet packing asymmetry, thus lowering the energetic barrier for the transition from partial insertion to fully formed pores. In contrast, high curvature imposes geometric constraints and increases the membrane deformation energy required for pore expansion, limiting the conformational rearrangement of αSO.[46−48]

Overall, our findings reveal that while αSO recruitment is curvature-promoted, pore formation dominates significantly in lower-curvature membranes, hence the two steps are decoupled, supporting our proposed three-stage model consisting of initial membrane binding followed by reversible cycling between partial insertion and subsequent full pore formation (Figure 4d).

Nanobodies Modify the Dynamics of αSO Pore Formation. The toxicity of αSOs suggests that interfering

https://doi.org/10.1021/acsnano.5c04005
ACS Nano 2025, 19, 32108−32122

with αSO-mediated membrane permeabilization or perforation could provide a therapeutic opportunity. Our single-particle approach enabled us to test whether ligands binding to αSOs affect the dynamics of pore formation. We discover that NB1 enhances pore formation and increases translocation turnover, suggesting a more flexible αSO structure and dynamic membrane interactions.

To achieve this, we tested two novel nanobodies, which, to our knowledge, are the only NBs that exhibit exclusive preference for αSOs and not the monomeric or fibrillar species.[21] First, we investigate the interaction between αSOs and NBs using TEM. Binding of NB1 resulted in a blurred and less defined αSO structure, whereas NB2 resulted in a population resembling free αSO (Figure 5a and Supplementary Figure 26). This difference may stem from the distinct binding affinities of the two nanobodies, as previously determined by Flow-Induced Dispersion Analysis (FIDA) and Surface Plasmon Resonance (SPR),[21] where NB1 shows stronger interaction with αSOs compared to NB2. Mass photometry further revealed broader and more variable mass distributions upon NB1 binding, consistent with increased conformational heterogeneity. Attempts to obtain high-resolution structures of the αSO:NB1 complex were unsuccessful, likely due to the formation of heterogeneous particle populations.[21]

Given the substantial changes observed upon NB1 binding, we next evaluated the binding using our real-time single-vesicle recording assay, as described in Figure 3. Fluorescently labeled αSO was added after 3 min by continuous flow for 4 min at a low rate to allow membrane saturation followed by NB addition after 10 min (Figure 5c and Supplementary Figure 27). NB1 addition resulted in a fluorescent quenching of the αSO, enabling the measurement of the NB1 binding rate (Supplementary Figures 27−28). Surprisingly, no difference in binding rate was observed across liposome sizes or αSO densities (Supplementary Figure 29). In contrast, NB2 addition did not result in fluorescent quenching (Supplementary Figure 28).

To evaluate the influence of NB1 and NB2 binding to αSO, we employed our real-time single-vesicle pore translocation recordings, as described in Figure 3. Here, we prepared three distinct oligomer samples: αSO incubated with NB1 (αSO:NB1), αSO incubated with NB2 (αSO:NB2), and αSO chemically modified with 4-oxo-2-nonenal (ONE:αSO), which stabilizes the structure, improving purification yield, but also alters structural and membrane interaction properties.[49] The data were compared with translocation results obtained from DOPG vesicles to facilitate statistical comparison. Interestingly, binding of NB1 resulted in a significant increase of pore formation, with 62.85 ± 7.15% of vesicles translocating compared to 35.16 ± 16.55% in absence of NBs (Figure 5d and Supplementary Figure 30). The pore formation is decreased for vesicles with αSO:NB2 to 25.67 ± 18.17% of the vesicles. The ONE-αSO significantly reduced pore formation, with 2.10 ± 1.60% liposomes exhibiting translocation. We observed that both NB1 and NB2 caused a significant upward shift in curvature dependency for the pore-forming events (Figure 5e) (P-value = 0.0054 and 8.32×10^{-62} MWU-test and P-value = 0.058 and 3.99×10^{-58} KS-test). Notably, the shift for αSO:NB1 is markedly reduced, indicating NB1 has a stronger impact on pore formation in curved membranes.

Again, the real-time resolution allowed us to analyze the NB effect on translocation turnovers as a function of liposome size (Figure 5f). Here, the fit from the absence of NB (from Figure 4b) is overlaid (black line) to compare the effects of the nanobodies (red line). NB1 changes the properties of αSOs, increasing the growth rate in the exponential fit from 0.003 to 0.009. Thus, larger liposomes with less curved membranes are more susceptible to frequent translocation. In contrast, NB2 does not result in any detectable changes. Additionally, we quantified the quantity of the lumen dyes translocated per event (Figure 5g) compared to conditions without NB (black line). We find that NB1 slightly decreased the correlation between percent dye translocation and liposome diameter, reducing the Spearman coefficient from 0.36 to 0.31, as expected due to elevated translocation frequency. Again, NB2 does not result in any detectable changes. Taken together, NB1 significantly enhanced pore formation and increased translocation turnover, suggesting a less stable or more flexible αSO structure that enables more dynamic membrane interactions. The chemically modified ONE-αSO showed significantly reduced pore formation, again suggesting that a more rigid αSO structure prevents the dynamic membrane interaction essential for pore formation.

CONCLUSIONS

Here, we developed a single-vesicle screening platform that enables the construction of a comprehensive biophysical model of membrane interactions for toxic αSO in unprecedented detail. We demonstrated real-time molecular translocation through αSO pores, visualized at single-vesicle resolution, and employed single-channel electrical recordings to analyze pore formation in planar lipid bilayers. By integrating data from various methods, we propose a novel three-stage model for αSO-membrane interactions consisting of initial membrane recruitment followed by reversible cycling between partial insertion and full pore formation.

Our single-vesicle data reveal that initial recruitment is both lipid- and charge-dependent, with a notable curvature-promoted effect. Using real-time single-vesicle imaging, we elucidate how individual αSOs become fully integrated into membranes and function as pores, translocating small molecules across membranes. Negative membrane charge plays a key role in pore incorporation. Strikingly, while αSO recruitment favors curved membranes, pore formation predominantly occurs in less curved membranes, which also allow more frequent release. This suggests that recruitment is independent of the ability for membrane reorientation, and that pore integration is specifically promoted by charge and lipid headgroup properties.

Our real-time single-vesicle recordings provide dynamic insights, revealing that individual liposomes undergo multiple translocations. The number of translocations positively correlates with liposome size, highlighting the highly dynamic nature of pore formation cycling between partial insertion to full pore formation. This process is modulated by membrane composition, with pore formation being more pronounced and appearing to be more stable in anionic DOPG vesicles compared to anionic DOPS vesicles. Interestingly, pore formation can be influenced by oligomer-binding nanobodies. One of the nanobodies significantly increased pore formation and enhanced dynamics, suggesting an altered αSO structure that enhances membrane interaction.

Our results indicate that pore formation can be modulated by lipid composition and ligands, offering a biophysical understanding of αSO toxicity and providing a platform to

https://doi.org/10.1021/acsnano.5c04005
ACS Nano 2025, 19, 32108−32122

screen for ligands that alter αSO structure and potentially mitigate PD-related cellular dysfunction.

Few studies have investigated αSO membrane recruitment, often relying on bulk measurements or qualitative methods that fail to capture the intrinsic heterogeneity of the recruitment process.[23,24] To our knowledge, the only single vesicle study on αSO recruitment did not detect binding of αSO to the POPC membranes of giant unilamellar vesicles but clearly showed binding to DOPG and DOPS membranes.[24] However, a microfluidic bulk study detected αSO recruitment to DOPC membranes of SUVs and LUVs, consistent with our observations of αSO recruitment by DOPC membranes.[23] However, the previous study was limited to only two groups of vesicle sizes and provided only bulk data. Additionally, our setup enables direct, real-time measurements, explicitly demonstrating that αSOs form pores.

The differential effects of DOPG and DOPS on αSO recruitment and pore formation likely originate from fundamental differences in headgroup structure and associated membrane properties. Although both lipids carry a net negative charge, the DOPS headgroup features a zwitterionic serine moiety capable of intramolecular hydrogen bonding, resulting in a more compact, rigid structure with reduced conformational flexibility. This rigidity limits headgroup mobility, reducing surface charge exposure. In contrast, the DOPG headgroup is smaller, anionic, and more conformationally flexible, providing a more accessible surface for electrostatic interaction and insertion.[50−52] These differences might explain why DOPG membranes promote greater αSO binding and more stable pore formation. In short, this is likely due to increased membrane defects and exposed hydrophobic regions, which facilitate deeper insertion and lateral organization of αSO.

The pronounced differences in αSO behavior on DOPG versus DOPS membranes are of potential biological significance since PG is a key lipid component of mitochondrial membranes, while PS is abundant in synaptic vesicles and confined to the cytoplasmic leaflet of the neuronal plasma membrane and thus can contribute to the understanding of PD-related cellular dysfunction. These results align with prior observations of monomeric α-synuclein interactions, suggesting that the N-terminus functions similarly but, in this case, facilitates pore insertion.[26]

The pore-forming ability of αSO has been suggested multiple times based on structural analysis[53,54] and vesicle permeabilization studies.[8,24,27,53,55] Here, we provide evidence for pore formation using highly sensitive single-channel planar bilayer measurements. A previous study demonstrated real-time pore formation in GUV vesicles,[27] speculated to be driven by transient nonequilibrium processes. However, limited data prevents firm conclusions. It has also been shown that oligomer-membrane interactions can be inhibited,[56] supporting our suggested three-stage model, in which recruitment does not necessarily lead to pore formation.

Our in vitro system offers a controlled platform to resolve the mechanistic details of α-synuclein pore formation that are difficult to access in vivo due to biological complexity and limited resolution. However, this model does not fully capture the dynamic and heterogeneous nature of in vivo membranes, such as diverse protein interactions, complex lipid compositions, and intercellular communication. While these limitations are inherent to in vitro approaches, they also enable a biophysical understanding of the interactions at an unprecedented level of detail. This model may further serve as a platform to investigate underlying mechanisms and to screen for molecules that inhibit small-molecule translocation or pore formation. Future in vivo studies will be important to assess how the pore formation is affected by more physiologically relevant conditions.

Importantly, our assay enables high-throughput screening of lipid compositions and curvatures and provides a direct and sensitive method for screening additives such as nanobodies. This could facilitate the identification of crucial ligands that bind to αSOs, potentially mitigating PD-related cellular dysfunction. More broadly, this assay establishes a framework to carry out comprehensive membrane-protein interaction analysis for protein aggregates in neurodegenerative disease. Tau protein aggregation, a hallmark of Alzheimer's disease, has been suggested to permeabilize lysosomes,[57] yet a detailed membrane-protein interaction analysis remains lacking. The real-time single-vesicle platform enables screening at millisecond resolution and allows observations extending up to several days. Studies on the internalization of preformed fibrils have shown that α-synuclein aggregates can perforate endolysosomes in neurons.[58] However, real-time single-vesicle analysis of synthetic membranes mimicking endolysosomes, or isolated endolysosomes themselves, is currently lacking and is essential for a comprehensive biophysical understanding. Such insights could pave the way for therapeutic interventions to prevent endolysosomal damage.

METHODS

Materials. Unless otherwise stated, all lipids and liposome extruder parts were acquired from Avanti Polar Lipids (Alabaster, Alabama, USA). Fluorophores, including fluorophore-conjugated lipids, were bought from ATTO-TEC GmbH (Siegen, Germany). Phosphate-buffered saline (PBS) was purchased from VWR (VWR International, Radnor, PA). For measurements containing $CaCl_2$, PBS and the desired amount of $CaCl_2$ stock were mixed to a final concentration of 1.2 mM $CaCl_2$. All water was type 1 grade produced by Milli-Q water purification system unless stated otherwise, and all solvents.

Expression and Purification of α-Syn and αSO. Expression and purification of α-synuclein (α-Syn) followed the protocol described by Paslawski et al.[30] Wild-type (WT) α-Syn was expressed in *Escherichia coli* BL21(DE3) cells containing the plasmid vector pET11a. Initially, cells were cultured on ampicillin-containing agar plates at 37 °C overnight. Subsequently, they were transferred to an autoinduction medium and incubated at 37 °C for 6 h, followed by harvest via centrifugation at 4500 rpm and 4 °C for 20 min. The resulting cell pellets were resuspended in osmotic shock buffer (30 mM Tris-HCl, 40% sucrose, 2 mM EDTA, pH 7.2) and subjected to centrifugation at 7000*g* and 20 °C for 30 min. After collection, the pellets were dissolved in ice-cold water supplemented with 40 μL of saturated $MgCl_2$ per 100 mL of medium while maintained on ice. The supernatant, obtained by centrifuging the dissolved pellets at 9000*g* and 4 °C for 30 min, was then adjusted to pH 3.5 with HCl. After centrifugation at 9000*g* and 4 °C for 20 min, the soluble proteins were collected in the supernatant, followed by adjustment of pH to 7.5 and storage at −80 °C.

The solution was subsequently filtered through a 0.22 μm filter before being loaded onto a Q-Sepharose column (3 × 5 mL HiTrap Q HP) with a 20 mM Tris-HCl buffer at pH 7.5 for equilibration, followed by elution using a buffer containing 20 mM Tris-HCl and 1 M NaCl. Elution was carried out with a gradient of elution buffer ranging from 0 to 50%. Fractions containing α-Syn were collected and subjected to SDS-PAGE analysis to confirm protein purity (Supplementary Figure 1a). Pure fractions were pooled, dialyzed against Milli-Q (MQ) water, lyophilized, and stored at −20 °C.

https://doi.org/10.1021/acsnano.5c04005
ACS Nano 2025, 19, 32108−32122

αSOs were prepared by diluting lyophilized α-Syn to a concentration of 622−691 μM in phosphate-buffered saline (PBS), followed by filtration using a 0.2 μm pore size syringe filter. The solution was then incubated in a Heating Shaking Dry bath (ThermoFisher Scientific) at 37 °C for 3−5 h. Prior to injection into the ÄKTA, the samples were centrifuged at 12,000*g* for 5 min to remove large aggregates. After equilibration of a Superose 6 gel filtration column with PBS, αSO was eluted at a flow rate of 0.75 mL/min. Fractions containing αSO (Supplementary Figure 1c), were pooled and concentrated using a 100 kDa Amicon Ultra-4 cutoff conical ultrafiltration unit (Merck Millipore Ltd., Tullagreen, Co., Cork, Ireland) at 4 °C before storage at −20 °C. Protein purity was reassessed using SDS-PAGE (Supplementary Figure 1a). All αSO concentrations are expressed in terms of moles of monomers.

Expression and Purification of Nanobodies. Expression and purification of nanobodies followed the protocol described by Nielsen et al.[21] A BL21 *E. coli* strain was transformed with a pET11d vector encoding either nanobody-1 (NB1) or nanobody-2 (NB2). Transfected *E. coli* cells were plated on agar plates containing Lysogeny broth (LB) medium supplemented with 2% glycerol and 1 mM $MgCl^2$, followed by overnight incubation at 37 °C. Colonies were then transferred to flasks containing LB medium supplemented with 0.1 mg/mL ampicillin and incubated for 2 h at 37 °C with agitation at 150 rpm using an Innova44 incubator shaker (New Brunswick, USA).

Induction of protein expression was initiated by adding 1 mM IPTG when the optical density (OD) of the culture reached 0.8, followed by further incubation for 4 h at 37 °C with agitation at 150 rpm. Subsequently, the cells were harvested by centrifugation at 4000 rpm for 20 min at 4 °C, and the resulting pellets were resuspended in 50 mL of NB buffer (50 mM Tris pH 8, 150 mM NaCl) supplemented with a proteinase inhibitor tablet (Roche, 05 892 791 001) and DNase (Sigma, 9003−98−9).

After sonication (6 cycles of 20 s each), the suspension was centrifuged for 20 min at 10,000*g* at 4 °C, and the supernatant containing the expressed nanobodies was collected. The supernatant was then loaded onto a Histrap HP 1 mL column pre-equilibrated with NB buffer using a GE ÄKTA Pure system (ÄKTA, USA). Nanobodies were eluted from the column using a gradient of NB buffer containing 0.5 M imidazole. Fractions containing nanobodies were collected and desalted using a PD10 column. The purity of the nanobodies was assessed by SDS-PAGE (Supplementary Figure 1a).

To facilitate storage, 10% glycerol was added to the samples, which were then stored at −80 °C.

Dot Blot of α-Synuclein Species. To verify the purification and isolation of off-pathway αSO, we used two highly specific nanobodies that selectively detect our αSO species, in contrast to a previously published antibody. The procedure was as follows:

Monomer, oligomer, fibril, and ONE oligomer samples were diluted to 10, 2, and 1 mg/mL. We spotted 5 μL of each sample onto membranes, which were blocked in 1× PBS with 2% BSA for 30 min. Membranes were washed three times in PBS with 0.05% Tween 20, then incubated for 1 h at room temperature (50 rpm on a Thermo Scientific rolling table) with 3 mL of nanobody solution (5 μg/mL in PBS). After three washes in PBS with 0.05% Tween 20, membranes were incubated for 1 h at room temperature (50 rpm) with 3 mL of primary His antibody (1 μg/mL in PBS; Sigma-Aldrich SAB2702218) and washed again three times.

Next, membranes were incubated with secondary antibody (Jackson GAM-HRP, 1:20,000 in PBS) for 1 h at room temperature (50 rpm), followed by three washes. Membranes were stained with 2−3 mL TMB blotting solution (Kementec) for 10 min at room temperature. After drying, arrays were scanned using a Bio-Rad GelDoc Go Imaging System.

For membranes without nanobody detection, α-synuclein samples were processed identically, using primary antibody 149E7A1 (1 μg/mL)[33] and the same secondary antibody and TMB staining protocol.

α-Synuclein Oligomer Labeling. Labeling of αSO with ATTO 655 was done by mixing 150 μL of αSO (34.5781−69.1563 μM), 50 μL of 1 M bicarbonate, and 30 μL of 1.13 mM ATTO 655 NHS ester followed by 2 h incubation on ice. Subsequently, the solution was centrifuged in a 100 kDa Amicon Ultra-4 cutoff conical ultrafiltration unit (Merck Millipore Ltd., Tullagreen, Co., Cork, Ireland) to get rid of the unconjugated dye. The labeled αSO was stored at −20 °C.

αSO-ATTO655 fluorescence was measured in the presence of NB on Cary Eclipse fluorescence spectrometer (Agilent Technologies, Santa Clara, CA) with excitation at 640 nm and emission at 655 and 850 nm. Spectra were recorded with slit widths of 10 nm (excitation) and 10 nm (emission) at 20 °C.

Liposome Preparation. The preparation of liposomes was done according to an earlier described protocol.[28,59] A series of unilamellar vesicles were prepared using 1,2-dioleoyl-*sn*-glycero-3-phospho-L-serine (DOPS), 1,2-Dioleoyl-*sn*-glycero-3-phosphocholine (DOPC), 1,2-Dioleoyl-*sn*-glycero-3-phosphoglycerol (DOPG), 0.5% 1,2-distearoyl-*sn*-glycero-3-phosphoethanolamine-N-[biotinyl(polyethylene glycol)-2000] (DSPE-PEG(2000) Biotin), and 0.5% ATTO488- 1,2-Dioleoyl-*sn*-glycero-3-phosphoethanolamine (DOPE). The lipid composition ranged from 0 to 99% DOPG and 0 to 99% DOPS. The remaining lipids, up to 100% were the neutral DOPC lipids. All lipid stocks were stored in chloroform at −20 °C and mixed in glass vials. Chloroform was evaporated under a stream of N_2, followed by an hour of incubation in a vacuum to form a lipid film. Liposomes were formed by rehydrating the film in phosphate-buffered saline (PBS) (VWR International, Radnor, PA) containing 1.2 mM $CaCl_2$ and allowed to self-assemble in the dark for 30 min.

The liposomes underwent ten cycles of flash-freezing and thawing to ensure unilamellar vesicles, followed by extrusion through a 200 nm Nuclepore Track-Etch membrane (GE Healthcare, Uppsala, Sweden) using an Avanti mini-extruder (Avanti Polar lipids Inc., Alabama, USA). Liposomes were stored at 4 °C for a maximum of 2 weeks from preparation to imaging.

Liposomes with encapsulated molecules were made as described, with the following additions to the protocol, and described earlier.[28,43] The rehydration buffer contained either 200 μM ATTO 488-dextran 4 kDa (TdBLabs, Uppsala, Sweden), 600 μM ATTO655 carboxy, or 600 μM ATTO488 carboxy. In the case of ATTO 488-dextran 4 kDa, ATTO488-DOPE was replaced with ATTO655, and for ATTO488 carboxy, no membrane dye was used.

Acquisition of TIRF Microscopy Data. Glass slides were cleaned by 10 min of sonication in 3× 2% Helmanex, 3× Milli-Q water, and 1× methanol. The cleaned glass surfaces were prepared using plasma-cleaned and activated precleaned glass slices with attached Sticky-Slide VI 0.4 (Ibidi GmbH, Gräfelfing, Germany) and functionalized with PLL-*g*-PEG and PLL-*g*-PEG-biotin in a 100:1 ratio and incubated for 30 min. Excess PLL-*g*-PEG and PLL-*g*-PEG-biotin were removed by washing each well, followed by addition of a 0.1 g/L neutravidin layer. Excess neutravidin was removed by washing each well with PBS.

Biotinylated liposomes were introduced into the system and allowed to immobilize, resulting in approximately 400 vesicles per field of view (FOV). Unbound liposomes were removed by washing with 3× chamber volumes of buffer.

A solution of 100 μL of 0.01 μM αSO-ATTO655 (0.31 μM αSM concentration) was added to the chamber and allowed to incubate for 10 min, after which unbound αSOs were removed by washing 5 times with PBS containing 1.2 mM CaCl2. Imaging was conducted both before and after the addition of αSO using 7 × 7 images with 200 μm spacing between the centers of each FOV in an automated fashion. For real-time detection of encapsulated molecule leakage, time-lapse was made with a temporal resolution of 1 image/min in a single FOV for 5 h. A Shenchen labv1 peristaltic flow pump (Baoding Shenchen Precision Pump Co., Ltd., Baodin, China) was integrated into the system for automatic αSO flow. Seven minutes into the acquisition, 0.3 mL of 0.01 μM αSO (0.31 μM αSM concentration) was infused into the system with a flow rate of 0.07 mL/min. For real-time detection of bound αSO 1 nM (50 nM αSM concentration) αSO was used.

All single-particle experiments were performed using an Oxford Nanoimager S (Oxford NanoImaging, Oxford, UK), an inverted total internal reflection fluorescence microscope. Data were acquired using a 100× 1.41 NA oil-immersion objective at room temperature (19

https://doi.org/10.1021/acsnano.5c04005
ACS Nano 2025, 19, 32108−32122

°C). Imaging utilized two solid-state lasers at 488 and 640 nm, and images were acquired with alternating lasers with laser powers set at 3.35% (<0.1 mW) and 5% (0.1 mW) and an exposure time of 200 or 50 ms. Image dimensions for each channel were 428 × 684 pixels with a dynamic range of 16-bit grayscale, recording 2 channels simultaneously. With a pixel size of 117 nm, the physical field of view (FOV) had dimensions of 50 μm × 80 per channel.

TIRF Real-time Detection of NB Binding. Glass slide preparation and liposome binding as described in the previous section. Images were acquired with a temporal resolution of 1 s for approximately 23 min. Images were acquired with alternating lasers with an exposure time of 200 ms. After 3 min from start acquisition 0.3 mL 0.01 mM αSO (0.31 μM αSM concentration) was infused into the system. Subsequently, 10 min after start acquisition 0.3 mL 3.1 mM nanobody was infused into the system both were done with a flow rate of 0.07 mL/min by a peristaltic pump.

Transmission Electron Microscopy (TEM). A nanobody-binding antigen-binding fragment (NabFab) was conjugated to the nanobody in a ratio of 1:3. NB:NabFab was mixed with αSO in a 10:1 ratio.

Carbon-coated 400 mesh copper grids were glow-discharged and 5 μL sample was added. The grids were washed with one drop of distilled water and stained with one drop of 1% uranyl formate for negative staining (ns). The solution was blotted and dried. Electron microscopy was done on a Tecnai G2 Spirit (FEI company) and images were taken using a TemCam F416 camera (TVIPS). The sample protocol was used for both NB1 and NB2.

Experimental Setup for Electrical Recordings of Pore Formation. To investigate pore insertion behaviors of αSO, we conducted electrical recordings using a setup involving vertical planar lipid membranes, following the established protocols.[42,60] In summary, we employed either 1,2-diphytanoyl-*sn*-glycero-3-phosphocholine (DPhPC) or 1,2-dihexadecanoyl-*sn*-glycero-3-phosphoglycerol (DPhPG) to create a lipid bilayer on the Teflon film aperture within the chamber. The chamber was connected to a patch-clamp amplifier (Axopatch 200B, Axon Instruments) via two electrodes with an anode on the trans side and a cathode on the cis side. Each side of the chamber was filled with 1 mL of electrolyte buffer (1 M KCl, 50 mM Tris, pH 7.4), with or without the supplementation of 1.5 mM $CaCl_2$. Varying concentrations of α-Syn monomer/oligomer were added to the trans side of the chamber, and a voltage of +20 mV was applied for all the measurements. All recordings were conducted at a sampling frequency of 10 kHz and a room temperature of around 25 °C.

Nanoparticle Tracking Analysis (NTA). The hydrodynamic radius of the liposomes was determined using a NanoSight LM10 system (Malvern Instruments Ltd., Malvern, UK), fitted with a high sensitivity cCMOS camera (OrcaFlash2.8, Hamamatsu C11440, NanoSight Ltd.) and a 405 nm laser. Each sample was diluted 1:1000 in PBS and measured in triplicate of 30-s recordings with a camera level of 11 and a detection threshold of 3. Videos were recorded and analyzed using the NTA software (version 3.1, build 3.1.45). The ambient temperature was recorded manually and was approximately 20 °C.

The relationship between the square root of the integrated signal from the membrane and liposome size is well-established, demonstrating a log-normal distribution of sizes as anticipated. By utilizing the average liposome size determined through Nanoparticle Tracking Analysis (NTA), it is possible to translate membrane intensity measurements into liposome sizes expressed in nanometers.[36]

Data Analysis. *Identification and Colocalization Software for TIRF Multiplexing Still Imaging.* The identification and colocalization of all liposomes and αSO were conducted using the membrane signal from the ATTO-488-DOPE membrane dye and colocalized to the αSO-ATTO-655 signal using in-house developed Python software, which was modified from recently published articles.[28,43,59] Each target was identified by using a Laplacian of Gaussian approximation, followed by selecting a region of interest (ROI) and a reference outer annulus to make an accurate local background correction. The software was designed to achieve nanometer-precise localization and colocalization across multiple imaging channels, effectively compensating for potential drifts caused by continuous fluid flow.

For each liposome formulation, the distribution of the colocalized αSO signal was square root transformed and fitted with a Gaussian distribution to obtain the mean and std. The data was normalized to the intensity before adding αSO, which enabled us to normalize to the overall shifts in liposome formulation.

Identification and Colocalization Software for TIRF Multiplexing Real-time Assay. Real-time measurements were saved as a stack of still images, where Identification and colocalization for each image in the stack were performed as described for the still imaging. After this, the localized targets were connected through the z-stack using a Linear Assignment Problem Tracker (LAP Tracker), creating a time-resolved trajectory. This was done by using in-house developed Python software, which was modified from recently published articles.[28,43,59]

By streamlining the tracking and analysis process, our software supports detailed investigations into the dynamics of liposome and αSO interactions, crucial for advancing our understanding of nanoscale biological processes.

Statistical Significance. We used the Mann−Whitney *U* test to compare the shift in mean since it does not assume normality and allows for heterogeneity of variance. A Kolmogorov−Smirnov test was used to compare whether two independent samples come from the same distribution, examining the differences in the entire distribution. The *P*-values for all statistical tests in the main text and the Supporting Information are $^{*}P \leq 0.05$, $^{**}P \leq 0.01$, and $^{***}P \leq 0.001$.

ASSOCIATED CONTENT

Data Availability Statement

Data supporting the findings of this study are available here https://anon.erda.au.dk/sharelink/F2mNpbWMlb. All raw data are available upon request. Software code for treatment of single vesicle data and statistical analysis is available here: https://anon.erda.au.dk/sharelink/gnKqxEmisl.

Supporting Information

The Supporting Information is available free of charge at https://pubs.acs.org/doi/10.1021/acsnano.5c04005.

Additional figures and data supporting the findings of this study are available online. These include purification procedures for nanobodies and α-synuclein (Figure S1); dot blot analysis of α-synuclein (Figure S2); nanoparticle tracking analysis and liposome size distribution before and after αSO addition (Figures S3−S5); intensity shift profiles in 640 channels upon αSO addition (Figures S6 and S7); surface coating controls and quantification of αSO recruitment to liposome membranes (Figures S8−S10); real-time single-vesicle recordings demonstrating αSO pore formation and molecular translocation under various conditions (Figures S11−S16); current trajectories and I−V curves showing αSO insertion and pore formation on planar lipid bilayers with and without $CaCl_2$ (Figures S17−S24); encapsulation of fluorescent dyes in liposomes (Figures S25) nsTEM imaging of α-syn oligomers, nanobody binding dynamics and signal quenching (Figures S26−S28); quantification of αSO recruitment and nanobody interactions (Figure S29); and real-time recordings of αSO pore formation in the presence of nanobodies (Figure S30) (PDF)

https://doi.org/10.1021/acsnano.5c04005
ACS Nano 2025, 19, 32108−32122

AUTHOR INFORMATION

Corresponding Authors

Daniel E. Otzen − *Interdisciplinary Nanoscience Center (iNANO), Aarhus University, 8000 Aarhus C, Denmark; Department of Molecular Biology and Genetics, Aarhus University, 8000 Aarhus C, Denmark;* orcid.org/0000-0002-2918-8989; Email: dao@inano.au.dk

Mette Galsgaard Malle − *Interdisciplinary Nanoscience Center (iNANO), Aarhus University, 8000 Aarhus C, Denmark;* orcid.org/0000-0003-3722-502X; Email: malle@inano.au.dk

Authors

Bo Volf Brøchner − *Interdisciplinary Nanoscience Center (iNANO), Aarhus University, 8000 Aarhus C, Denmark*

Xialin Zhang − *Interdisciplinary Nanoscience Center (iNANO), Aarhus University, 8000 Aarhus C, Denmark*

Janni Nielsen − *Interdisciplinary Nanoscience Center (iNANO), Aarhus University, 8000 Aarhus C, Denmark*

Jørgen Kjems − *Interdisciplinary Nanoscience Center (iNANO), Aarhus University, 8000 Aarhus C, Denmark; Department of Molecular Biology and Genetics, Aarhus University, 8000 Aarhus C, Denmark*

Complete contact information is available at: https://pubs.acs.org/10.1021/acsnano.5c04005

Notes

A preprint of this manuscript was previously uploaded as B.V.B.; X.Z.; J.N.; J.K.; D.E.O.; M.G.M.; Single-vesicle tracking of α-synuclein oligomers reveals pore formation by a three-stage model modulated by charge, curvature, lipids and ligands. 2025, 10.1101/2025.04.10.648112, bioRxiv, 10.1101/2025.04.10.648112 (accessed July 22, 2025).

The authors declare no competing financial interest.

ACKNOWLEDGMENTS

This work was funded by Lundbeck Foundation grant No. R380-2021-1393 for M.G.M. Danish National Research Foundation grant no. 135 (CellPAT) for B.V.B., X.Z., and J.K. Lundbeck foundation grant No. R276-2018-671 and R453-2024-359 for J.N. and D.E.O.

REFERENCES

(1) Auluck, P. K.; Caraveo, G.; Lindquist, S. α-Synuclein: membrane interactions and toxicity in Parkinson's disease. *Annual review of cell and developmental biology* **2010**, *26* (1), 211−233.

(2) Cookson, M. R. α-Synuclein and neuronal cell death. *Mol. Neurodegeneration* **2009**, *4*, 9.

(3) Musteikytė, G.; Jayaram, A. K.; Xu, C. K.; Vendruscolo, M.; Krainer, G.; Knowles, T. P. Interactions of α-synuclein oligomers with lipid membranes. *Biochimica et Biophysica Acta (BBA)-Biomembranes* **2021**, *1863* (4), No. 183536.

(4) Mor, D. E.; Ugras, S. E.; Daniels, M. J.; Ischiropoulos, H. Dynamic structural flexibility of α-synuclein. *Neurobiology of disease* **2016**, *88*, 66−74.

(5) Leverenz, J. B.; Umar, I.; Wang, Q.; Montine, T. J.; McMillan, P. J.; Tsuang, D. W.; Jin, J.; Pan, C.; Shin, J.; Zhu, D. Proteomic identification of novel proteins in cortical lewy bodies. *Brain Pathol.* **2007**, *17* (2), 139−145.

(6) Alam, P.; Bousset, L.; Melki, R.; Otzen, D. E. α-synuclein oligomers and fibrils: a spectrum of species, a spectrum of toxicities. *Journal of neurochemistry* **2019**, *150* (5), 522−534.

(7) Giehm, L.; Svergun, D. I.; Otzen, D. E.; Vestergaard, B. Low-resolution structure of a vesicle disrupting α-synuclein oligomer that accumulates during fibrillation. *Proc. Natl. Acad. Sci. U. S. A.* **2011**, *108* (8), 3246−3251.

(8) Volles, M. J.; Lansbury, P. T. Vesicle permeabilization by protofibrillar α-synuclein is sensitive to Parkinson's disease-linked mutations and occurs by a pore-like mechanism. *Biochemistry* **2002**, *41* (14), 4595−4602.

(9) van Rooijen, B. D.; Claessens, M. M.; Subramaniam, V. Lipid bilayer disruption by oligomeric α-synuclein depends on bilayer charge and accessibility of the hydrophobic core. *Biochimica et Biophysica Acta (BBA)-Biomembranes* **2009**, *1788* (6), 1271−1278.

(10) Emin, D.; Zhang, Y. P.; Lobanova, E.; Miller, A.; Li, X.; Xia, Z.; Dakin, H.; Sideris, D. I.; Lam, J. Y.; Ranasinghe, R. T. Small soluble α-synuclein aggregates are the toxic species in Parkinson's disease. *Nat. Commun.* **2022**, *13* (1), 5512.

(11) Awasthi, S.; Ying, C.; Li, J.; Mayer, M. Simultaneous determination of the size and shape of single α-synuclein oligomers in solution. *ACS Nano* **2023**, *17* (13), 12325−12335.

(12) Roberts, H. L.; Brown, D. R. Seeking a mechanism for the toxicity of oligomeric α-synuclein. *Biomolecules* **2015**, *5* (2), 282−305.

(13) Lorenzen, N.; Otzen, D. E. Oligomers of α-synuclein: picking the culprit in the line-up. *Essays in Biochemistry* **2014**, *56*, 137−148.

(14) Chen, S. W.; Drakulic, S.; Deas, E.; Ouberai, M.; Aprile, F. A.; Arranz, R.; Ness, S.; Roodveldt, C.; Guilliams, T.; De-Genst, E. J. Structural characterization of toxic oligomers that are kinetically trapped during α-synuclein fibril formation. *Proc. Natl. Acad. Sci. U. S. A.* **2015**, *112* (16), E1994−E2003.

(15) Lorenzen, N.; Nielsen, S. B.; Buell, A. K.; Kaspersen, J. D.; Arosio, P.; Vad, B. S.; Paslawski, W.; Christiansen, G.; Valnickova-Hansen, Z.; Andreasen, M. The role of stable α-synuclein oligomers in the molecular events underlying amyloid formation. *J. Am. Chem. Soc.* **2014**, *136* (10), 3859−3868.

(16) Paslawski, W.; Andreasen, M.; Nielsen, S. B.; Lorenzen, N.; Thomsen, K.; Kaspersen, J. D.; Pedersen, J. S.; Otzen, D. E. High stability and cooperative unfolding of α-synuclein oligomers. *Biochemistry* **2014**, *53* (39), 6252−6263.

(17) Asaadi, Y.; Jouneghani, F. F.; Janani, S.; Rahbarizadeh, F. A comprehensive comparison between camelid nanobodies and single chain variable fragments. *Biomark. Res.* **2021**, *9*, 87.

(18) Muyldermans, S. Nanobodies: natural single-domain antibodies. *Annual review of biochemistry* **2013**, *82*, 775−797.

(19) Caljon, G.; Caveliers, V.; Lahoutte, T.; Stijlemans, B.; Ghassabeh, G. H.; Van Den Abbeele, J.; Smolders, I.; De Baetselier, P.; Michotte, Y.; Muyldermans, S. Using microdialysis to analyse the passage of monovalent nanobodies through the blood−brain barrier. *Br. J. Pharmacol.* **2012**, *165* (7), 2341−2353.

(20) Muruganandam, A.; Tanha, J.; Narang, S.; Stanimirovic, D. Selection of phage-displayed llama single-domain antibodies that transmigrate across human blood-brain barrier endothelium. *FASEB J.* **2002**, *16* (2), 1−22.

(21) Nielsen, J.; Pedersen, J. N.; Kleijwegt, G.; Nowak, J. S.; Nami, F.; Johansen, C.; Sassetti, E.; Berg, B. B.; Lyngsø, N. M.; Brøchner, B. V. Nanobodies raised against the cytotoxic α-synuclein oligomer are oligomer-specific and promote its cellular uptake. *npj Biosensing* **2025**, *2* (1), 23.

(22) van Maarschalkerweerd, A.; Vetri, V.; Vestergaard, B. Cholesterol facilitates interactions between α-synuclein oligomers and charge-neutral membranes. *FEBS letters* **2015**, *589* (19), 2661−2667.

(23) Šneiderienė, G.; Czekalska, M. A.; Xu, C. K.; Jayaram, A. K.; Krainer, G.; Arter, W. E.; Peter, Q. A.; Castellana-Cruz, M.; Saar, K. L.; Levin, A. α-Synuclein oligomers displace monomeric α-synuclein from lipid membranes. *ACS Nano* **2024**, *18* (27), 17469−17482.

(24) van Rooijen, B. D.; Claessens, M. M.; Subramaniam, V. Membrane binding of oligomeric α-synuclein depends on bilayer charge and packing. *FEBS letters* **2008**, *582* (27), 3788−3792.

(25) Volles, M. J.; Lee, S.-J.; Rochet, J.-C.; Shtilerman, M. D.; Ding, T. T.; Kessler, J. C.; Lansbury, P. T. Vesicle permeabilization by protofibrillar α-synuclein: implications for the pathogenesis and

treatment of Parkinson's disease. *Biochemistry* **2001**, *40* (26), 7812−7819.
(26) Hannestad, J. K.; Rocha, S.; Agnarsson, B.; Zhdanov, V. P.; Wittung-Stafshede, P.; Höök, F. Single-vesicle imaging reveals lipid-selective and stepwise membrane disruption by monomeric α-synuclein. *Proc. Natl. Acad. Sci. U. S. A.* **2020**, *117* (25), 14178−14186.
(27) van Rooijen, B. D.; Claessens, M. M.; Subramaniam, V. Membrane permeabilization by oligomeric α-synuclein: in search of the mechanism. *PLoS One* **2010**, *5* (12), No. e14292.
(28) Malle, M. G.; Löffler, P. M.; Bohr, S. S.-R.; Sletfjerding, M. B.; Risgaard, N. A.; Jensen, S. B.; Zhang, M.; Hedegård, P.; Vogel, S.; Hatzakis, N. S. Single-particle combinatorial multiplexed liposome fusion mediated by DNA. *Nat. Chem.* **2022**, *14* (5), 558−565.
(29) Schmidt, S. G.; Malle, M. G.; Nielsen, A. K.; Bohr, S. S.-R.; Pugh, C. F.; Nielsen, J. C.; Poulsen, I. H.; Rand, K. D.; Hatzakis, N. S.; Loland, C. J. The dopamine transporter antiports potassium to increase the uptake of dopamine. *Nat. Commun.* **2022**, *13* (1), 2446.
(30) Paslawski, W.; Lorenzen, N.; Otzen, D. E. Formation and characterization of α-synuclein oligomers. *Protein Amyloid Aggregation: Methods and Protocols* **2016**, *1345*, 133−150.
(31) Otzen, D. E. Antibodies and α-synuclein: What to target against Parkinson's Disease? *Biochim. Biophys. Acta Proteins Proteom.* **2024**, *1872* (2), No. 140943.
(32) Lorenzen, N.; Lemminger, L.; Pedersen, J. N.; Nielsen, S. B.; Otzen, D. E. The N-terminus of α-synuclein is essential for both monomeric and oligomeric interactions with membranes. *FEBS letters* **2014**, *588* (3), 497−502.
(33) Nielsen, J.; Lauritsen, J.; Pedersen, J. N.; Nowak, J. S.; Bendtsen, M. K.; Kleijwegt, G.; Lusser, K.; Pitarch, L. C.; Moreno, J. V.; Schneider, M. M. Molecular properties and diagnostic potential of monoclonal antibodies targeting cytotoxic α-synuclein oligomers. *NPJ Parkinsons Dis.* **2024**, *10* (1), 139.
(34) Hatzakis, N. S.; Bhatia, V. K.; Larsen, J.; Madsen, K. L.; Bolinger, P.-Y.; Kunding, A. H.; Castillo, J.; Gether, U.; Hedegård, P.; Stamou, D. How curved membranes recruit amphipathic helices and protein anchoring motifs. *Nat. Chem. Biol.* **2009**, *5* (11), 835−841.
(35) Kunding, A. H.; Mortensen, M. W.; Christensen, S. M.; Stamou, D. A fluorescence-based technique to construct size distributions from single-object measurements: application to the extrusion of lipid vesicles. *Biophys. J.* **2008**, *95* (3), 1176−1188.
(36) Lohr, C.; Kunding, A. H.; Bhatia, V. K.; Stamou, D. Constructing size distributions of liposomes from single-object fluorescence measurements. *Methods Enzymol.* **2009**, *465*, 143−160.
(37) Jo, E.; McLaurin, J.; Yip, C. M.; George-Hyslop, P. S.; Fraser, P. E. α-Synuclein membrane interactions and lipid specificity. *J. Biol. Chem.* **2000**, *275* (44), 34328−34334.
(38) Cui, H.; Lyman, E.; Voth, G. A. Mechanism of membrane curvature sensing by amphipathic helix containing proteins. *Biophysical journal* **2011**, *100* (5), 1271−1279.
(39) Nuscher, B.; Kamp, F.; Mehnert, T.; Odoy, S.; Haass, C.; Kahle, P. J.; Beyer, K. α-Synuclein has a high affinity for packing defects in a bilayer membrane: a thermodynamics study. *J. Biol. Chem.* **2004**, *279* (21), 21966−21975.
(40) Kang, C.; Sun, R. Molecular dynamics study of the interaction between the N-terminal of α-synuclein and a lipid bilayer mimicking synaptic vesicles. *J. Phys. Chem. B* **2021**, *125* (4), 1036−1048.
(41) Middleton, E. R.; Rhoades, E. Effects of curvature and composition on α-synuclein binding to lipid vesicles. *Biophysical journal* **2010**, *99* (7), 2279−2288.
(42) Zhang, X.; Galenkamp, N. S.; van der Heide, N. J.; Moreno, J.; Maglia, G.; Kjems, J. Specific Detection of Proteins by a Nanobody-Functionalized Nanopore Sensor. *ACS Nano* **2023**, *17* (10), 9167−9177.
(43) Zhang, X.; Malle, M. G.; Thomsen, R. P.; Sørensen, R. S.; Sørensen, E. W.; Hatzakis, N. S.; Kjems, J. Deconvoluting the Effect of Cell-Penetrating Peptides for Enhanced and Controlled Insertion of Large-Scale DNA Nanopores. *ACS Appl. Mater. Interfaces* **2024**, *16* (15), 18422−18433.
(44) Quist, A.; Doudevski, I.; Lin, H.; Azimova, R.; Ng, D.; Frangione, B.; Kagan, B.; Ghiso, J.; Lal, R. Amyloid ion channels: a common structural link for protein-misfolding disease. *Proc. Natl. Acad. Sci. U. S. A.* **2005**, *102* (30), 10427−10432.
(45) Lim, L.; Wenk, M. Neuronal membrane lipids−their role in the synaptic vesicle cycle. In *Handbook of neurochemistry and molecular neurobiology*, 3 ed.; Springer: Boston, MA, 2009.
(46) Thomsen, R. P.; Malle, M. G.; Okholm, A. H.; Krishnan, S.; Bohr, S. S.-R.; Sørensen, R. S.; Ries, O.; Vogel, S.; Simmel, F. C.; Hatzakis, N. S. A large size-selective DNA nanopore with sensing applications. *Nat. Commun.* **2019**, *10* (1), 5655.
(47) Akimov, S. A.; Volynsky, P. E.; Galimzyanov, T. R.; Kuzmin, P. I.; Pavlov, K. V.; Batishchev, O. V. Pore formation in lipid membrane II: Energy landscape under external stress. *Sci. Rep.* **2017**, *7* (1), 12509.
(48) Damm, A.; Paik, S.-J.; Sadhu, R. K.; Di-Cicco, A.; Manzi, J.; Castellana, M.; Margeat, E.; Dahan, M.; Sens, P.; Lévy, D.Conformational changes of the ABC Transporter BmrA Depend on Membrane Curvature. *bioRxiv* 2024, Version 2
(49) Andersen, C.; Grønnemose, A. L.; Pedersen, J. N.; Nowak, J. S.; Christiansen, G.; Nielsen, J.; Mulder, F. A.; Otzen, D. E.; Jørgensen, T. J. Lipid peroxidation products HNE and ONE promote and stabilize alpha-synuclein oligomers by chemical modifications. *Biochemistry* **2021**, *60* (47), 3644−3658.
(50) Kiskis, J.; Horvath, I.; Wittung-Stafshede, P.; Rocha, S. Unraveling amyloid formation paths of Parkinson's disease protein α-synuclein triggered by anionic vesicles. *Q. Rev. Biophys.* **2017**, *50*, No. e3.
(51) Bacle, A.; Buslaev, P.; Garcia-Fandino, R.; Favela-Rosales, F.; Ferreira, T. M.; Fuchs, P. F.; Gushchin, I.; Javanainen, M.; Kiirikki, A. M.; Madsen, J. J. Inverse conformational selection in lipid−protein binding. *J. Am. Chem. Soc.* **2021**, *143* (34), 13701−13709.
(52) Büldt, G.; Wohlgemuth, R. The headgroup conformation of phospholipids in membranes. *J. Membr. Biol.* **1981**, *58*, 81−100.
(53) Lashuel, H. A.; Petre, B. M.; Wall, J.; Simon, M.; Nowak, R. J.; Walz, T.; Lansbury, P. T., Jr α-Synuclein, especially the Parkinson's disease-associated mutants, forms pore-like annular and tubular protofibrils. *Journal of molecular biology* **2002**, *322* (5), 1089−1102.
(54) Fusco, G.; Chen, S. W.; Williamson, P. T.; Cascella, R.; Perni, M.; Jarvis, J. A.; Cecchi, C.; Vendruscolo, M.; Chiti, F.; Cremades, N. Structural basis of membrane disruption and cellular toxicity by α-synuclein oligomers. *Science* **2017**, *358* (6369), 1440−1443.
(55) Ghio, S.; Camilleri, A.; Caruana, M.; Ruf, V. C.; Schmidt, F.; Leonov, A.; Ryazanov, S.; Griesinger, C.; Cauchi, R. J.; Kamp, F. Cardiolipin promotes pore-forming activity of alpha-synuclein oligomers in mitochondrial membranes. *ACS Chem. Neurosci.* **2019**, *10* (8), 3815−3829.
(56) Lorenzen, N.; Nielsen, S. B.; Yoshimura, Y.; Vad, B. S.; Andersen, C. B.; Betzer, C.; Kaspersen, J. D.; Christiansen, G.; Pedersen, J. S.; Jensen, P. H. How Epigallocatechin Gallate Can Inhibit α-Synuclein Oligomer Toxicity in Vitro. *J. Biol. Chem.* **2014**, *289* (31), 21299−21310.
(57) Rose, K.; Jepson, T.; Shukla, S.; Maya-Romero, A.; Kampmann, M.; Xu, K.; Hurley, J. H. Tau fibrils induce nanoscale membrane damage and nucleate cytosolic tau at lysosomes. *Proc. Natl. Acad. Sci. U. S. A.* **2024**, *121* (22), No. e2315690121.
(58) Sanyal, A.; Scanavachi, G.; Somerville, E.; Saminathan, A.; Nair, A.; Bango Da Cunha Correia, R. F.; Aylan, B.; Sitarska, E.; Oikonomou, A.; Hatzakis, N. S.; Kirchhausen, T. Neuronal constitutive endolysosomal perforations enable α-synuclein aggregation by internalized PFFs. *J. Cell Biol.* **2024**, *224* (2), No. e202401136.
(59) Malle, M. G.; Song, P.; Löffler, P. M.; Kalisi, N.; Yan, Y.; Valero, J.; Vogel, S.; Kjems, J. Programmable RNA Loading of Extracellular Vesicles with Toehold-Release Purification. *J. Am. Chem. Soc.* **2024**, *146* (18), 12410−12422.
(60) Maglia, G.; Heron, A. J.; Stoddart, D.; Japrung, D.; Bayley, H. Analysis of single nucleic acid molecules with protein nanopores. In *Methods in enzymology*; Elsevier, 2010; *475*; 591−623.

https://doi.org/10.1021/acsnano.5c04005
ACS Nano 2025, 19, 32108−32122